Chemical Science

ROYAL SOCIETY OF CHEMISTRY

EDGE ARTICLE

View Article Online
View Journal

Cite this: DOI: 10.1039/d5sc10091g

All publication charges for this article have been paid for by the Royal Society of Chemistry

A rigid donor unit strategy enables highly efficient narrowband blue multi-resonance thermally activated delayed fluorescence emitters

Deli Li, *[ac] Simin Jiang,[c] Qingchao Liu,[a] Ruizhe Xu,[a] Guo-Xi Yang,[c] Wei Li, *[b] Shi-Jian Su *[c] and Xuchuan Jiang *[a]

Received 24th December 2025
Accepted 9th February 2026

DOI: 10.1039/d5sc10091g

rsc.li/chemical-science

Benzothienocarbazole (BTC) regioisomers, featuring a relatively heavy sulfur atom, a rigid molecular structure, and moderate electron-donating ability, are used in the design of TADF emitters. Here, a comprehensive structural and optoelectronic investigation of two narrowband blue MR-TADF emitters with rigid donor units is presented. A *tert*-butyldiphenylamine group at the *para* position of the boron atom gives these molecules a hybrid frontier molecular orbital distribution, showing both short-range charge transfer (SRCT) and long-range charge transfer (LRCT) traits. The rigid donor units not only diminish the high-frequency vibronic coupling strength of the commonly involved stretching modes but also lower the non-radiative decay rate constants of the triplet state. Consequently, these two emitters produce narrowband blue emissions with full width at half maximum (FWHM) values below 23 nm and high photoluminescence quantum yields over 90%. Non-sensitized OLEDs based on BTC-BN and BFC-BN exhibit blue emissions centered at 476 and 478 nm, with FWHMs of 31 and 29 nm, respectively, and maximum EQEs of 30.9% and 27.7%, respectively. This highlights the unique advantages and importance of the rigid donor in controlling the excited state and enhancing device performance.

Introduction

Multi-resonance thermally activated delayed fluorescence (MR-TADF) materials have attracted significant attention due to their considerable potential for various applications in high-resolution organic light-emitting diode (OLED) displays. Unlike traditional TADF emitters that depend on twisted donor–acceptor (D–A) structures, MR-TADF emitters are characterized by a rigid polycyclic aromatic hydrocarbon (PAH) molecular structure.[1–4] This design markedly diminishes structural relaxation in the excited state, thereby facilitating narrowband emission and achieving high photoluminescence quantum yields (PLQYs). Furthermore, the MR effect induced by boron and nitrogen atoms at the para position within the PAH frameworks facilitates efficient spatial separation of the highest occupied molecular orbital (HOMO) and the lowest unoccupied molecular orbital (LUMO). This leads to a reduced singlet–triplet splitting energy (ΔE_{ST}s). Additionally, the intrinsic rigidity of MR-TADF materials minimizes vibrational relaxation and reduces Stokes shifts, leading to narrowband emission. Consequently, MR-TADF emitters can effectively harness both singlet and triplet excitons for light emission, achieving high efficiency *via* efficient reverse intersystem crossing (RISC) and narrowband electroluminescence (EL) spectra in devices. Accordingly, numerous MR-TADF molecules exhibiting narrowband emission and high external quantum efficiency (EQE), spanning deep blue to deep red, have been reported using this strategy.[5–8]

However, due to the relatively inefficient RISC process with a low RISC rate (κ_{RISC}) of 10^3–10^4 s^{-1} for MR-TADF emitters, significant efficiency roll-off can be observed in their devices, which limits their practical industrial application. In terms of material design, researchers have proposed a variety of molecular design strategies. Yang *et al.* proposed a pragmatic approach to introduce a multichannel RISC pathway with large spin–orbit coupling (SOC) by orthogonally linking an electron-donating unit to the MR framework.[9] These merits enabled a high maximum EQE of up to 37.1% and alleviated efficiency roll-off in the sensitizer-free device. To reduce the ΔE_{ST}s of MR-TADF emitters and accelerate the κ_{RISC}, extending the π-skeleton of MR-TADF materials has been proposed.[10–12] According to this strategy, κ_{RISC} can be accelerated to 10^6 s^{-1}. The heavy atom effect (HAE) is an effective means of overcoming this issue, as it can significantly enhance the SOC, thereby increasing κ_{RISC}.[13–20] For example, Yasuda *et al.* reported a blue-emitting MR emitter

[a]*Institute for Smart Materials & Engineering, University of Jinan, Jinan, 250022, P. R. China. E-mail: ism_lidl@ujn.edu.cn; ism_jiangxc@ujn.edu.cn*

[b]*Zhejiang Provincial Engineering Research Center of Energy Optoelectronic Materials and Devices, Ningbo Institute of Materials Technology and Engineering, Chinese Academy of Sciences, Ningbo 315201, P. R. China. E-mail: liwei1987@nimte.ac.cn*

[c]*Guangdong Basic Research Center of Excellence for Energy and Information Polymer Materials, Institute of Polymer Optoelectronic Materials and Devices, State Key Laboratory of Luminescent Materials and Devices, South China University of Technology, Guangzhou 510640, P. R. China. E-mail: mssjsu@scut.edu.cn*

doped with a sulfur or selenium atom in the BN framework, which exhibited a high κ_{RISC} and enabled minimal efficiency roll-off in EL devices.[15,16] Yang *et al.* designed a series of MR emitters incorporating heavy atoms by integrating phenothiazine (PXZ) or phenoselenazine (PSeZ) moieties into the MR system.[13,18] These emitters exhibited rapid κ_{RISC} of 2.0×10^6 s^{-1}, resulting in EL devices with an efficiency of up to 36.8% and remarkably low efficiency roll-off. Traditional methods usually involve directly adding heavy atoms into the MR core, which limits the scope for further molecular design innovations. Furthermore, adding bridging heavy atoms such as sulfur or selenium can cause significant local distortions in the excited state, thereby improving structural relaxation and reducing color purity.[21]

Benzothienocarbazole (BTC) regioisomeric moieties, featuring a moderately heavy sulfur atom, a rigid molecular framework, and moderate electron-donating ability, have been used in the design of TADF emitters.[22,23] The molecular rigidity of these emitters is substantially enhanced, which effectively suppresses intramolecular vibrational and rotational motions, thereby minimizing nonradiative decay pathways and facilitating radiative photon emission. In our prior research, we proposed the construction of MR scaffolds using rigid sulfur-containing donor groups, namely 7*H*-benzo[4,5]thieno[2,3-*b*]carbazole. As a result, an organic boron emitter (BTC-BNCz) capable of high-efficiency, low-efficiency roll-off, and narrowband TADF emission (λ_{EL} = 496 nm) was developed.[23] Benefitting from the heavy atom effect of the sulfur atom and rigid structure of the molecule, accelerated κ_{RISC} of 1.6×10^5 s^{-1} and high efficiency of 35.2% were achieved with narrowband emission and slow efficiency roll-off. Subsequently, Wang *et al.* explored the implications of regioisomerism on SOC, focusing on the relative position of the benzothienocarbazole with respect to the MR-TADF core and its effect on κ_{RISC}.[20] Results show that the molecules with the 12*H*-benzo[4,5]thieno[2,3-*a*]carbazole donor unit exhibited relatively higher SOCME than corresponding molecules with the 5*H*-benzo[4,5]thieno[3,2-*c*]carbazole donor unit. A maximum EQE of 34.9% was achieved, demonstrating reduced efficiency roll-off. These emitters exhibited blue-green emission with the emission peaked at 491–496 nm in OLED. In 2025, Wang and Liang *et al.* reported two green emitters by utilizing benzothienocarbazole groups with sulfur atoms connecting with the 3-position carbon atoms of carbazole units.[24] Ultimately, Th-Cz-BN3- and Th-Cz-BN6-based non-sensitized devices displayed pure green emission with peaks at 525 and 529 nm, along with FWHM of 30 and 29 nm, respectively. However, owing to the strong electron-donating character of the BTC regioisomeric moieties, the resulting MR-TADF emitters display blue-green or green emission (Fig. 1), which highlights the scarcity of blue-emitting MR-TADF emitters.

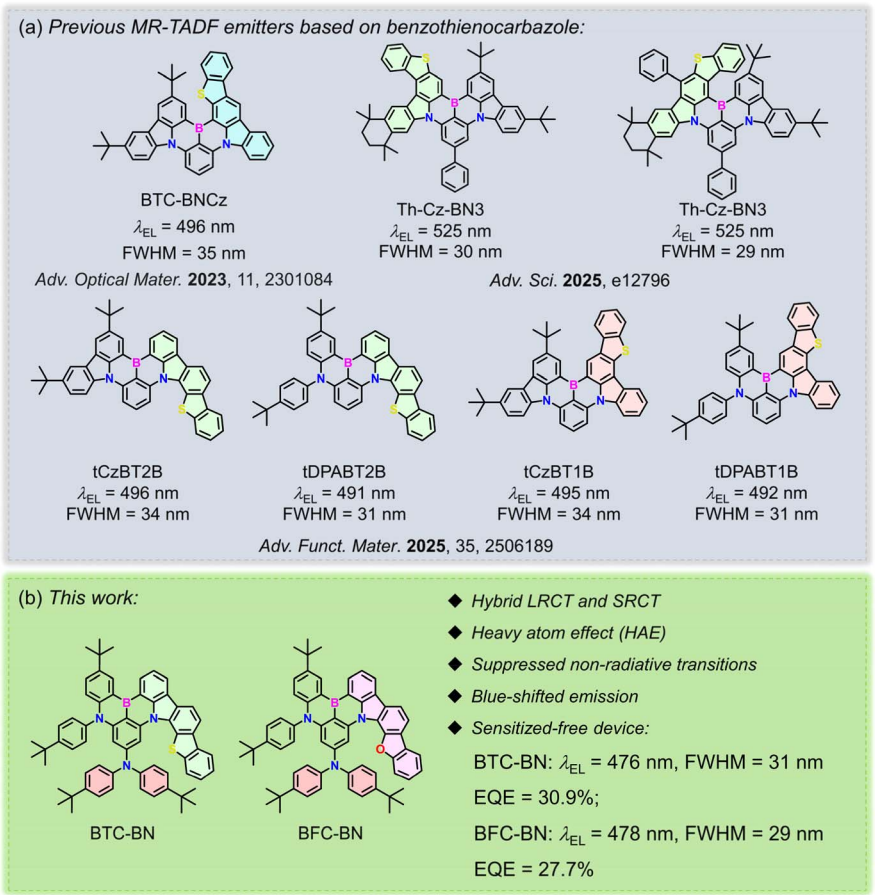

Fig. 1 (a) Previous MR-TADF emitters based on benzothienocarbazole. (b) The chemical structures and EL properties of BTC-BN and BFC-BN in this work.

Herein, a comprehensive structural and optoelectronic investigation is conducted on two narrowband blue MR-TADF emitters (Fig. 1), BTC-BN and BFC-BN, which possess 12*H*-benzo[4,5]thieno[2,3-*a*]carbazole (BTC) and 12*H*-benzofuro[2,3-*a*]carbazole (BFC) donor units, respectively. BTC and BFC units were selected as donors owing to their relatively deeper HOMO energy levels compared to other substituents, suggesting weaker electron-donating capabilities and making them favorable for the development of blue MR-TADF emitters. (Fig. S2) A *tert*-butyldiphenylamine (*t*-BuTPA) unit was introduced at the *para* position relative to the boron atom to attenuate the acceptor strength through B–π–N conjugation, leading to a hybrid frontier molecular orbital (FMO) distribution with both short-range charge transfer (SRCT) and long-range charge transfer (LRCT) characteristics for these two emitters. Consequently, the blue emission of these two emitters with the emission peaks at 469 and 472 nm in toluene for BTC-BN and BFC-BN, respectively, was observed. Owing to the rigid structures of the BTC and BFC units, resulting in reduced non-radiative triplet-state decay rate constants (κ_{nr}^{T}) on the order of 10^2, both emitters demonstrated high PLQYs exceeding 90% in thin films. Furthermore, the high-frequency vibronic coupling strength of the commonly involved stretching modes has been effectively suppressed, resulting in narrowband emission from BTC-BN and BFC-BN in toluene solution, with FWHM values of 23 and 22 nm, respectively. The presence of the heavy sulfur atom enhances the κ_{RISC} of BTC-BN, yielding a value of 5.5×10^4 s^{-1}. As a result, the devices based on these two emitters exhibited the maximum EQEs of 30.9% and 27.7% for BTC-BN- and BFC-BN-based sensitizer-free devices, with blue emission peaks at 476 and 478 nm, respectively, and FWHM values of 31 and 29 nm, respectively. This work underscores the critical role of the heavy-atom effect in enhancing the RISC process and its influence on the device performance of MR-TADF-based devices.

Results and discussion

Synthesis and thermal properties

The chemical structures of the designed emitters, namely BTC-BN and BFC-BN, are depicted in Fig. 1, and their synthetic routes are shown in the SI. Intermediates A1 and B1 were synthesized *via* the Ullmann coupling reaction. Subsequently, intermediates A2 and B2 were synthesized *via* the Buchwald–Hartwig coupling reaction. The target molecules were successfully prepared *via* a "one-pot" boronization method, driven by rationally increased electron density at the corresponding sites.[25,26] Molecular structures were confirmed by mass spectrometry (MS) and nuclear magnetic resonance (NMR) spectrometry. All target products were further purified by repeated temperature gradient vacuum sublimation. Furthermore, their thermal properties were measured by thermogravimetric analysis (TGA). As shown in Fig. S1, both molecules exhibited relatively high decomposition temperatures (T_d, 5% mass loss) of 496 and 481 °C, respectively, indicating good thermal stability that would benefit vacuum-deposition fabrication of OLED devices. Additionally, no obvious glass transition was observed below 350 °C for BTC-BN, whereas BFC-BN shows a glass transition temperature (T_g) of 85 °C, indicating that its thermal stability is sufficient to support application in evaporation processes.

Theoretical simulation

Initially, the electronic properties of the two materials were examined in depth using DFT and time-dependent DFT (TD-DFT) calculations at the PBE0/6-31G(d, p) level. As shown in Fig. 2, the LUMOs are distributed on the boron atom and its *ortho*- and *para*-positioned carbon atoms. At the same time, the HOMO mainly localizes on the nitrogen atoms and their *ortho*- and *para*-positioned carbon atoms, extending slightly onto the fused BTC and BFC moieties. This indicates well-separated, short-range HOMO/LUMO distributions, a typical feature of MR emitters. However, the HOMO distributions of both emitters extend into the B-*para tert*-butyldiphenylamine (*t*-BuTPA) units, suggesting significant long-range charge-transfer (LRCT) behavior. This orbital pattern makes these two emitters recognized as a hybrid frontier molecular orbital (FMO) distribution with both SRCT and LRCT characteristics. We then performed spin-component scaled second-order approximate coupled-cluster (SCS-CC2/cc-PVDZ) calculations to obtain accurate excited-state energies.[27,28] Results show that the ΔE_{ST} values for BTC-BN and BFC-BN were 0.16 and 0.15 eV, respectively, indicating the potential of the RISC process and delayed fluorescence in these two emitters. To clarify the emission nature, excited-state energy levels, and natural transition orbital (NTO) distributions, these quantities were theoretically estimated using TD-DFT calculations (Fig. S4 and S5). The $S_0 \rightarrow S_1$ excitation of BTC-BN is mainly contributed by HOMO → LUMO transitions with the weights of 82.9% and HOMO-1 → LUMO transitions with the weights of 14.4% (Fig. S2 and Table S2), displaying a high transition oscillator strength (*f*) value of 0.3128. However, $S_0 \rightarrow T_1$ excitation of BFC-BN is primarily contributed by HOMO-1 → LUMO (88.0%) and HOMO → LUMO transitions (9.0%)[29] with a high transition oscillator strength (*f*) value (0.3902). Clearly, the S_1 states of both emitters show a hybrid of LRCT and SRCT components. To study triplet-state delocalization in the compounds, triplet-state spin densities (TSDDs) were calculated (Fig. S6), revealing that the TSDDs of both emitters are localized on the MR core. This indicates that the MR core controls their triplet-state properties.

To investigate how the sulfur-containing material BTC-BN influences intersystem crossing (ISC) and reverse intersystem crossing (RISC) in molecular systems, we calculated the spin–orbit coupling (SOC) matrix elements between the S_1 state and the T_m ($m \leq 4$) state.[15,23,30] As shown in Fig. 2 and Table S1, for BTC-BN, considerably significant SOC matrix elements, $\langle S_1|\hat{H}_{SOC}|T_m\rangle$, ranging from 0.14 to 1.30 cm^{-1}, were estimated for the multiple $T_m \rightarrow S_1$ channels, which are higher than that of BFC-BN (Fig. 2). Thus, we envision that the involvement of the lone-pair (*n*) electrons from the sulfur atoms enables a weak direct spin-flip pathway between the T_1 and S_1 states. The large SOC of BTC-BN would be beneficial for excitonic spin-flipping excitonic. Moreover, these two molecules were found to possess the T_3 state located below the S_1 state, transformation, because RISC can be accelerated by providing an additional effective spin-flip pathway, as evidenced by the higher $\langle S_1|\hat{H}_{SOC}|T_m\rangle$ ($m = 3$ or 4) values. Likewise, the energetically close-

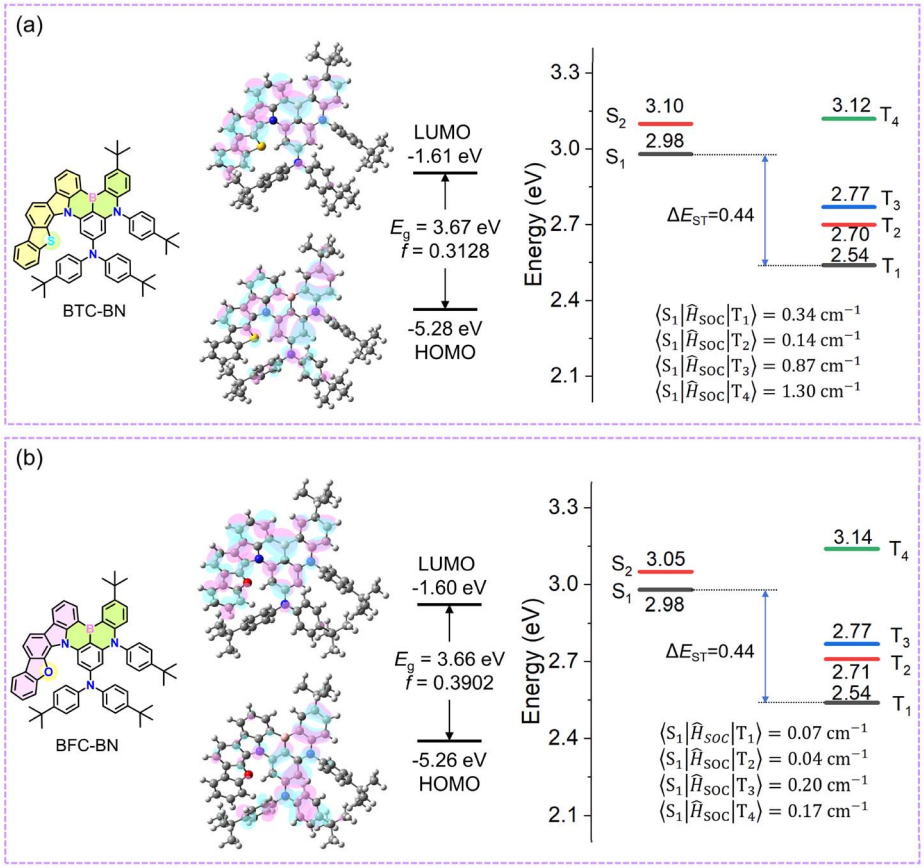

Fig. 2 Molecular structures, optimized ground state geometries, and the frontier molecular orbital distributions of the S_0 state, the energy levels, and spin orbital coupling matrix elements between the T_m and S_1 states for BTC-BN (a) and BFC-BN (b).

lying T_4 state and S_2 state may also contribute to the up-conversion process through the spin–vibronic mechanism, which can be confirmed by the $\langle S_2|\hat{H}_{SOC}|T_m\rangle$ ($m = 3$ or 4) values (Table S1).

To further deepen the understanding of the differences in bandwidth between the two compounds, the Huang–Rhys (HR) factors and reorganization energies for different vibrational modes were also calculated using the MOMAP program.[31,32] As shown in Fig. 3, these two emitters displayed similar vibration mode patterns, HR factors, and reorganization energies, indicating similar emission bandwidths. The reorganization energies of BTC-BN and BFC-BN were calculated to be 0.890 and 0.877 eV (Fig. 3a and S7), respectively. Such a small λ value corresponds to fewer vibrational modes that dissipate energy non-radiatively through structural relaxation, thereby enhancing the PLQY of the emitters and sharpening the emission spectrum. Furthermore, the geometry relaxation is dominated by low-frequency (<100 cm^{-1}) twisting vibrational modes, whereas high-frequency (>1000 cm^{-1}) vibrations are largely suppressed. The major vibrational modes at low vibration frequencies (12.57 cm^{-1} for BTC-BN and 9.52 cm^{-1} for BFC-BN) of both emitters were analyzed in detail, as shown in Fig. 3. The vibration modes at ≈10 cm^{-1} were mainly due to bending vibrations of the *t*-BuTPA units, resulting in narrowband emission spectra for these two molecules.

Photophysical properties

Ultraviolet-visible (UV-vis) absorption and photoluminescence (PL) spectra of BTC-BN and BFC-BN were measured in dilute toluene solutions (1×10^{-5} M). Fig. 4 shows that both materials display intense, sharp absorption bands peaking at 453 nm for BTC-BN and 458 nm for BFC-BN, indicating SRCT. The optical bandgaps (E_gs) were found to be 2.62 and 2.59 eV for BTC-BN and BFC-BN, respectively, based on the absorption onset. PL spectra demonstrate strong, sharp blue emissions with peaks at 469 nm for BTC-BN and 472 nm for BFC-BN, with small FWHMs of 23 and 22 nm, respectively, and Stokes shifts of 13 nm. These findings suggest minimal molecular–geometrical relaxation between the ground and excited states, due to their fully fused, rigid molecular structures. A slight positive solvatochromism (Fig. S8) supports the idea that the SRCT character of the S_1 state remains consistent across different solvents. To determine the ΔE_{ST} values of the two emitters, low-temperature fluorescence and phosphorescence spectra were measured at 77 K in a degassed frozen toluene matrix (Fig. S9). The singlet energies (E_{S1}s) were determined to be 2.77 eV for BTC-BN and 2.74 eV for BFC-BN, while the triplet energies (E_{T_1}s) were both 2.57 eV. The resulting ΔE_{ST} values are 0.20 eV for BTC-BN and 0.17 eV for BFC-BN, which agree well with the theoretical predictions from the SCS-CC2 method. Such low ΔE_{ST} values ensure

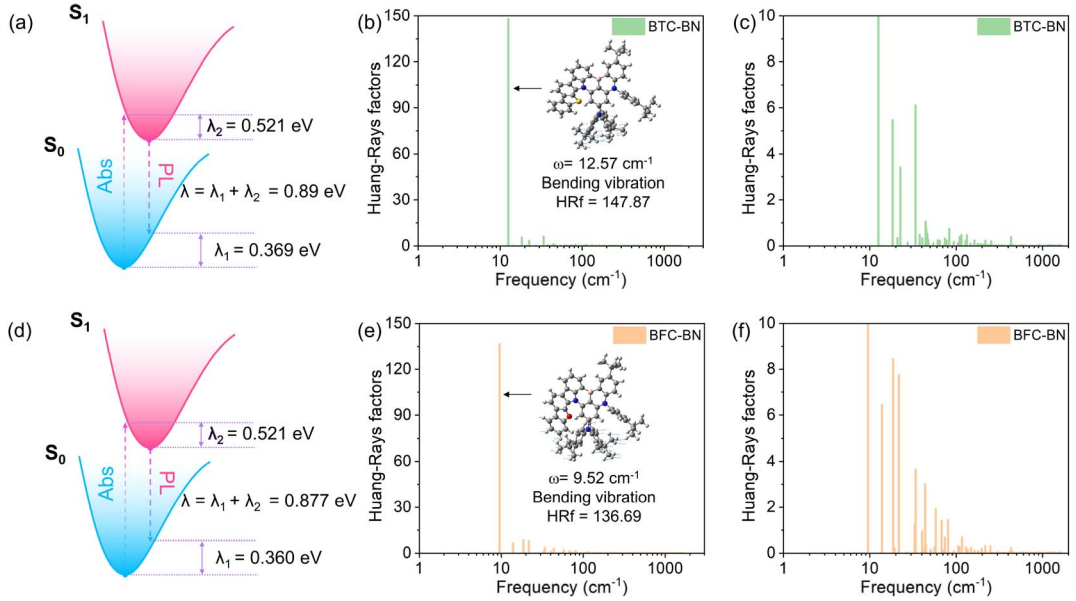

Fig. 3 Calculated reorganization energy (λ) and Huang–Rhys (HR) factor for the $S_1 \rightarrow S_0$ transition of BTC-BN (a–c) and BFC-BN (d–f) (inset: vibration modes with significant contributions to the Huang–Rhys factors).

efficient RISC and delayed fluorescence emission for BTC-BN and BFC-BN.

When doped at 3 wt% in the host 1,3-di(9*H*-[3,9′-bicarbazol]-9-yl)benzene (mBCP), both BTC-BN and BFC-BN exhibited emission spectra similar to those in toluene solution, though with a slight bathochromic shift. As shown in Fig. S11, the films exhibited blue emission peaking at 475 nm for BTC-BN and 478 nm for BFC-BN, with a FWHM of 28 nm for both. The redshifted and broadened emission spectra observed in the solid state in comparison with those in solution are attributed to three interrelated factors: solid-state solvation effects, π–π interactions between the host and dopant molecules, and conformational changes upon film formation.[20,23,33] Transient PL decay measurements conducted on the doped films at room temperature revealed biexponential decays (Fig. 4b), confirming TADF behavior. Prompt fluorescence lifetimes (τ_{PF}) were 3.8 ns for BTC-BN and 5.9 ns for BFC-BN, while the delayed components (τ_{DF}) were 50.3 μs and 88.7 μs, respectively. Key photophysical parameters, calculated following established literature procedures,[29,34] are summarized in Tables 1 and S6. PLQYs reached 96.8% for BTC-BN and 94.6% for BFC-BN under a nitrogen atmosphere. Both emitters exhibited fast singlet radiative decay rate constants (κ_r^S) of 9.0×10^7 s^{-1} for BTC-BN and 4.5×10^7 s^{-1} for BFC-BN. The non-radiative triplet decay rate constants (κ_{nr}^T) were relatively low, measured as 7.7×10^2 s^{-1} and 9.7×10^2 s^{-1}, respectively, indicating suppressed non-radiative triplet deactivation (Table 1).

Device performances

Before fabricating OLED devices, the levels of HOMOs and LUMOs were measured using ultraviolet photoelectron spectroscopy (Fig. S12), and the corresponding HOMO energy levels

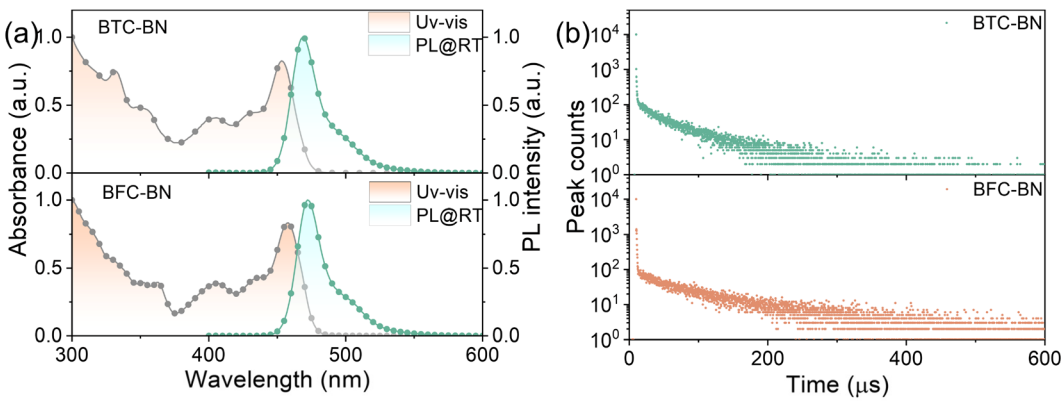

Fig. 4 (a) UV-vis absorption and PL spectra of BTC-BN and BFC-BN in toluene measured at room temperature (298 K). (b) Transient PL decay of BTC-BN and BFC-BN in the mBCP host matrix (3 wt%).

Table 1 Photophysics properties of BTC-BN and BFC-BN

Emitters	λ_{abs}[a] [nm]	λ_{em}[a] [nm]	FWHM[b] [nm]	E_g [eV]	HOMO/LUMO[c] [eV]	S_1/T_1[d] [eV]	ΔE_{ST}[d] [eV]	PLQY[e] [%]	τ_{PF}/τ_{DF}[f] [ns μs^{-1}]	κ_r^S [10^7 s^{-1}]	κ_{ISC} [10^8 s^{-1}]	κ_{RISC} [10^4 s^{-1}]	κ_{nr}^T [10^2 s^{-1}]	κ_{CQ} [10^2 s^{-1}]
BTC-BN	453	469	23	2.62	−5.47/−2.85	2.77/2.57	0.20	96.8	3.8/50.3	9.0	1.7	5.5	9.7	9.7
BFC-BN	458	472	22	2.59	−5.40/−2.81	2.74/2.57	0.17	94.6	4.7/88.7	4.5	1.7	5.0	7.7	7.8

[a] Measured in toluene (1×10^{-5} M, 298 K). [b] FWHM: full width at half maximum. [c] HOMO energy level was determined from ultraviolet photoelectron spectroscopy, LUMO = HOMO + E_g. [d] Singlet and triplet energy estimated from the onset of the fluorescence and phosphorescence spectrum in a frozen toluene matrix (1×10^{-5} M, 77 K), $\Delta E_{ST} = S_1 - T_1$. [e] Absolute photoluminescence quantum yield in 3 wt%-doped mBCP films. [f] Measured in mBCP doped film (3 wt%).

were estimated to be −5.47 and −5.40 eV for BTC-BN and BFC-BN, respectively (Fig. S12). The LUMO energy levels of these two materials are calculated to be −2.85 and −2.81 eV for BTC-BN and BFC-BN, respectively. Given the promising photophysics of BTC-BN and BFC-BN, the devices with the structure of ITO/HATCN (10 nm)/TAPC (30 nm)/mBCP: 3 wt% (20 nm)/TmPyPB (40 nm)/LiF (1 nm)/Al (150 nm) were prepared for exploring their EL properties. Here, indium tin oxide (ITO) and aluminum (Al) were used as the anode and cathode, respectively. 1,1-Bis(4-(*N*, *N*-di(*p*-tolyl)-amino)-phenyl)cyclohexane (TAPC) and 1,3,5-tri(*m*-pyrid-3-ylphenyl)benzene (TmPyPB) served as the hole- and electron-transporting layers, respectively. 1,4,5,8,9,11-hexaazatriphenylenehexacarbonitrile (HATCN) and LiF layers served as hole- and electron-injection layers, respectively. In the emission layer, mBCP was used as the host material due to its high triplet energy of 3.0 eV (Fig. S10 and Table S5) and good charge-transporting properties. The doping concentration of these two emitters was optimized to 3 wt%. The structures of the materials used for device fabrication, as well as the energy level diagram of the devices, are illustrated in Fig. 5.

The EL performance of devices incorporating BTC-BN and BFC-BN were systematically evaluated. Key device characteristics, including current density–voltage–luminance (*J*–*V*–*L*) curves, efficiency curves, and EL spectra, are presented in Fig. 5 and S13, with detailed parameters summarized in Table 2. The EL spectra of both devices closely align with their corresponding PL profiles, confirming minimal excited-state distortion in the electroluminescence process. The devices exhibit blue emission with peaks at 476 nm (BTC-BN) and 478 nm (BFC-BN), corresponding to CIE coordinates of (0.11, 0.22) and (0.11, 0.25), respectively. The observed spectral broadening (FWHM: 31 nm for BTC-BN, 29 nm for BFC-BN) relative to doped films is attributed to enhanced π–π stacking and host–dopant intermolecular interactions under electrical excitation.[23,35] Both the

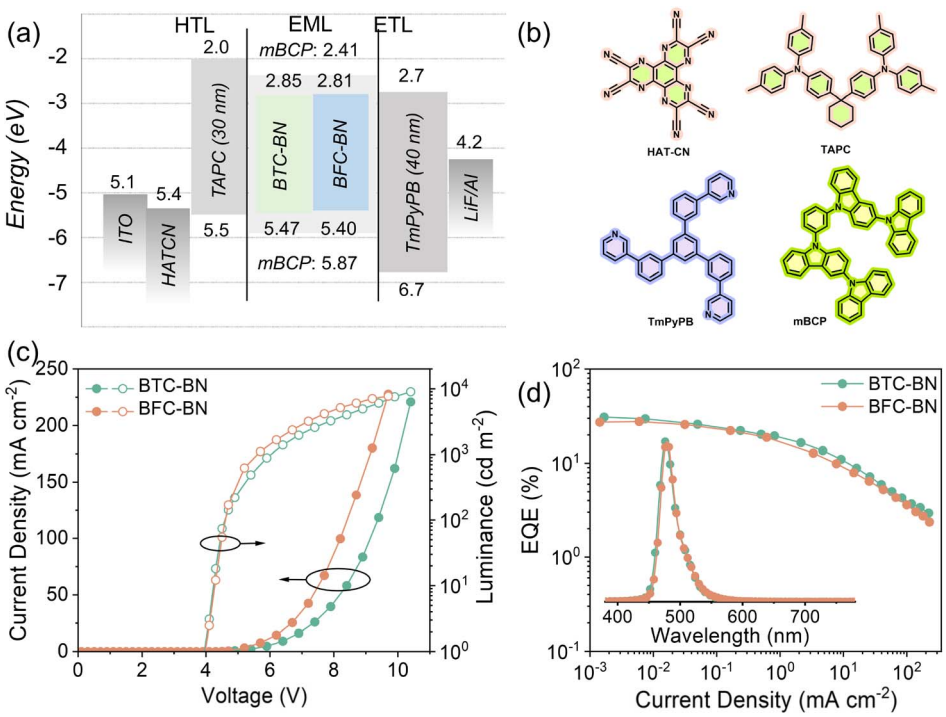

Fig. 5 (a) Device architecture and energy diagram for the devices. (b) Chemical structures of the molecules used in device fabrication. (c) Current density–voltage–luminance (*J*–*V*–*L*) curves. (d) Efficiency curves and the EL spectra (inset) of the devices based on BTC-BN and BFC-BN.

Table 2 OLED performance of BTC-BN and BFC-BN-based devices

Dopant	V_{on}[a] [V]	L_{max}[b] [cd m^{-2}]	CE[c] [cd A^{-1}]	PE[c] [lm W^{-1}]	EQE[c] [%]	FWHM[d] [nm]	λ_{EL}[e] [nm]	CIE[f] [x, y]
BTC-BN	4.0	8996	42.9	34.6	30.9	31	476	0.11, 0.22
BFC-BN	4.0	7720	41.6	31.8	27.7	29	478	0.11, 0.25

[a] Turn-on voltage at the luminance of 1 cd m^{-2}. [b] Maximum luminance. [c] Maximum external quantum efficiency, power efficiency and current efficiency. [d] Full-width at half maxima values. [e] EL peaks. [f] Commission Internationale de l'Eclairage (CIE) coordinates measured at 8 V.

devices displayed low turn-on voltages (V_{on}, at 1 cd m^{-2}) of 4.0 V and high luminance owing to a suitable energy cascade between functional layers (Fig. 4a). The device based on BTC-BN exhibited the best performance, with a maximum EQE of 30.9% and a maximum current efficiency of 34.6 cd A^{-1}, without employing any light-out-coupling enhancement. Furthermore, the device using BFC-BN as the emitter exhibited an EQE of 27.7% and a CE of 31.8 cd A^{-1}. Moreover, the rigidity of benzothienocarbazole suppresses molecular relaxation, leading to narrowband emission, high PLQY, and fast κ_r in the solid state. These results highlight the importance of the heavy-atom effect and a rigid donor in improving the RISC process and its impact on device performance in MR-TADF-based devices. Notably, both devices show low turn-on voltages ($V_{on} \approx 4.0$ V) and achieve high luminance, benefiting from a favorable energy-level cascade between the functional layers (Fig. 5a). Most significantly, the device based on BTC-BN delivered a maximum EQE of 30.9% and a current efficiency (CE) of 34.6 cd A^{-1} without any light-outcoupling enhancement, representing a remarkable result for a narrowband blue TADF emitter. The BFC-BN-based device also showed high performance, with an EQE of 27.7% and a CE of 31.8 cd A^{-1}. The superior efficiency of BTC-BN is consistent with its enhanced spin–orbit coupling and faster RISC processes, both of which are underpinned by the heavy-atom effect of the sulfur-rich donor. Moreover, the rigid benzothienocarbazole architecture effectively suppresses molecular relaxation, contributing to narrow emission bandwidths, high PLQY values, and rapid κ_r in the solid state. These results collectively underscore the effectiveness of combining a heavy-atom-promoted donor with a rigid molecular framework to facilitate RISC and achieve high-efficiency, narrowband blue TADF EL. The work demonstrates a viable molecular design strategy for advancing the performance of MR-TADF emitters in display applications.

Conclusions

To conclude, we have developed two narrowband blue MR-TADF emitters, BTC-BN and BFC-BN, using BTC and BFC donor units and B–π–N conjugated *t*-BuTPA donor units. A comprehensive structural and optoelectronic investigation of these donor units on the MR-TADF core and their effect on κ_{RISC} and SOCME was also examined. Due to the rigid structures of the BTC and BFC units, the high-frequency vibronic coupling of the commonly involved stretching modes has been effectively suppressed, resulting in narrowband emission from BTC-BN and BFC-BN in toluene solution, with FWHM values of 23 and 22 nm, respectively. The moderately heavy sulfur atom contributes to a larger SOCME value ($\langle S_1|\hat{H}_{SOC}|T_m\rangle$) of 0.34 cm^{-1} for BTC-BN, resulting in a higher κ_{RISC} of BTC-BN with a value of 5.5×10^4 s^{-1}. The manufactured sensitizer-free OLED device based on BTC-BN and BFC-BN exhibits blue emission at 476 and 478 nm, with FWHMs of 31 and 29 nm, respectively, and maximum EQEs of 30.9% and 27.7%, respectively. This work underscores the critical role of the heavy-atom effect in enhancing the RISC process and its influence on the device performance and efficiency roll-off of MR-TADF-based devices.

Author contributions

Deli Li: conceptualization, investigation, formal analysis, funding acquisition, visualization, writing – original draft, methodology. Simin Jiang: investigation, formal analysis. Qingchao Liu: investigation, visualization. Ruizhe Xu: investigation, visualization. Guo-Xi Yang: formal analysis, investigation, resources. Wei Li: writing – review & editing, supervision. Shi-Jian Su: writing – review & editing, supervision. Xuchuan Jiang: writing – review & editing, project administration.

Conflicts of interest

There are no conflicts to declare.

Data availability

The data that support this article are available in the article itself and its supplementary information (SI). Supplementary information: experimental methods, synthetic procedures and structural characterization data, theoretical calculations, thermodynamics data, photophysics data and device performance data. See DOI: https://doi.org/10.1039/d5sc10091g.

Acknowledgements

The authors greatly appreciate the National Natural Science Foundation of China (22305086, 22522512), and the Natural Science Foundation of Shandong Province (ZR2024QB123).

Notes and references

1 T. Hatakeyama, K. Shiren, K. Nakajima, S. Nomura, S. Nakatsuka, K. Kinoshita, J. Ni, Y. Ono and T. Ikuta, *Adv. Mater.*, 2016, **28**, 2777–2781.
2 N. Ikeda, S. Oda, R. Matsumoto, M. Yoshioka, D. Fukushima, K. Yoshiura, N. Yasuda and T. Hatakeyama, *Adv. Mater.*, 2020, **32**, e2004072.

3 Y. Kondo, K. Yoshiura, S. Kitera, H. Nishi, S. Oda, H. Gotoh, Y. Sasada, M. Yanai and T. Hatakeyama, *Nat. Photon.*, 2019, **13**, 678–682.
4 S. Madayanad Suresh, D. Hall, D. Beljonne, Y. Olivier and E. Zysman-Colman, *Adv. Funct. Mater.*, 2020, **30**, 1908677.
5 H. J. Cheon, S. J. Woo, S. H. Baek, J. H. Lee and Y. H. Kim, *Adv. Mater.*, 2022, **34**, e2207416.
6 L. Guo, W. Cui, L. Li, Y. Pu, K. Wang, P. Zheng, Y. Wang and C. Li, *Adv. Mater.*, 2025, **37**, e2500269.
7 J. J. Hu, Y. Wei, X. Z. Wang, X. Liang, X. J. Liao, L. Yuan, H. X. Ni and Y. X. Zheng, *Adv. Optical Mater.*, 2024, **12**, 2302987.
8 Y. Wang, Z. Ma, J. Pu, D. Guo, G. Li, Z. Chen, S. J. Su, H. Deng, J. Zhao and Z. Chi, *Aggregate*, 2024, **5**, e585.
9 Z. Huang, H. Xie, J. Miao, Y. Wei, Y. Zou, T. Hua, X. Cao and C. Yang, *J. Am. Chem. Soc.*, 2023, **145**, 12550–12560.
10 X. Lv, J. Miao, M. Liu, Q. Peng, C. Zhong, Y. Hu, X. Cao, H. Wu, Y. Yang, C. Zhou, J. Ma, Y. Zou and C. Yang, *Angew. Chem., Int. Ed.*, 2022, **61**, e202201588.
11 Y. C. Cheng, X. Tang, R. Walia, T. Y. Zhang, X. C. Fan, J. Yu, K. Wang, C. Adachi, X. K. Chen and X. H. Zhang, *Adv. Mater.*, 2025, **37**, e2500010.
12 J. R. Wu, Y. J. Yang, S. J. Ge, Y. K. Qu, H. Y. Yan, H. X. Jiang, Y. Liu, D. Y. Zhou, L. S. Liao and Z. Q. Jiang, *Adv. Funct. Mater.*, 2025, **35**, 2507553.
13 Y. X. Hu, J. S. Miao, T. Hua, Z. Y. Huang, Y. Y. Qi, Y. Zou, Y. T. Qiu, H. Xia, H. Liu, X. S. Cao and C. L. Yang, *Nat. Photon.*, 2022, **16**, 803–810.
14 I. S. Park, M. Yang, H. Shibata, N. Amanokura and T. Yasuda, *Adv. Mater.*, 2022, **34**, e2107951.
15 M. Nagata, H. Min, E. Watanabe, H. Fukumoto, Y. Mizuhata, N. Tokitoh, T. Agou and T. Yasuda, *Angew. Chem., Int. Ed.*, 2021, **60**, 20280–20285.
16 I. S. Park, H. Min and T. Yasuda, *Angew. Chem., Int. Ed.*, 2022, **61**, e202205684.
17 Y. Zou, M. Yu, Y. Xu, Z. Xiao, X. Song, Y. Hu, Z. Xu, C. Zhong, J. He, X. Cao, K. Li, J. Miao and C. Yang, *Chem*, 2024, **10**, 1485–1501.
18 X. Cao, K. Pan, J. Miao, X. Lv, Z. Huang, F. Ni, X. Yin, Y. Wei and C. Yang, *J. Am. Chem. Soc.*, 2022, **144**, 22976–22984.
19 Q. Li, Y. Wu, Q. Yang, S. Wang, S. Shao and L. Wang, *ACS Appl. Mater. Interfaces*, 2022, **14**, 49995–50003.
20 D. Y. Chen, H. Wang, F. Huang, D. B. Cordes, A. P. McKay, K. Wang, X. H. Zhang and E. Zysman-Colman, *Adv. Funct. Mater.*, 2025, **35**, 2506189.
21 T. Hua, L. S. Zhan, N. Q. Li, Z. Y. Huang, X. S. Cao, Z. Q. Xiao, S. L. Gong, C. J. Zhou, C. Zhong and C. L. Yang, *Chem. Eng. J.*, 2021, **426**, 131169.
22 M. Cai, M. Auffray, D. Zhang, Y. Zhang, R. Nagata, Z. Lin, X. Tang, C.-Y. Chan, Y.-T. Lee, T. Huang, X. Song, Y. Tsuchiya, C. Adachi and L. Duan, *Chem. Eng. J.*, 2021, **420**, 127591.
23 D. L. Li, M. K. Li, D. H. Liu, J. J. Yang, W. Li, Z. H. Yang, H. X. Yuan, S. M. Jiang, X. M. Peng, G. X. Yang, W. T. Xie, W. D. Qiu, Y. Y. Gan, K. K. Liu and S. J. Su, *Adv. Optical Mater.*, 2023, **11**, 2301084.
24 C. Jiang, Y. Nie, C. Cao, X. Song, J. Liang, X. Zhuang, Z. Li, B. Liang and Y. Wang, *Adv. Sci.*, 2026, **13**, e12796.
25 H. Hirai, K. Nakajima, S. Nakatsuka, K. Shiren, J. Ni, S. Nomura, T. Ikuta and T. Hatakeyama, *Angew. Chem., Int. Ed.*, 2015, **54**, 13581–13585.
26 D. Li, D. Liu, M. Li, Q. Liu, W. Liu, W. Li, S. J. Su and X. Jiang, *Chem. Sci.*, 2025, **16**, 18332–18340.
27 Y. J. Pu, D. Valverde, J. C. Sancho-Garcia and Y. Olivier, *J. Phys. Chem. A*, 2023, **127**, 10189–10196.
28 A. Pershin, D. Hall, V. Lemaur, J. C. Sancho-Garcia, L. Muccioli, E. Zysman-Colman, D. Beljonne and Y. Olivier, *Nat. Commun.*, 2019, **10**, 597.
29 D. Li, J. Yang, S. Jiang, H. Yuan, D. Liu, Z. Yang, G.-X. Yang, M. Li, X. Jiang, W. Li and S.-J. Su, *Chem. Eng. J.*, 2025, **504**, 158958.
30 Q. Zheng, Y.-K. Qu, P. Zuo, H.-T. Yuan, Y.-J. Yang, Y.-C. Qiu, L.-S. Liao, D.-Y. Zhou and Z.-Q. Jiang, *Chem*, 2025, **11**, 102353.
31 Y. Niu, W. Li, Q. Peng, H. Geng, Y. Yi, L. Wang, G. Nan, D. Wang and Z. Shuai, *Mol. Phys.*, 2018, **116**, 1078–1090.
32 Z. Shuai, H. Geng, W. Xu, Y. Liao and J. M. Andre, *Chem. Soc. Rev.*, 2014, **43**, 2662–2679.
33 P. Jiang, J. Miao, X. Cao, H. Xia, K. Pan, T. Hua, X. Lv, Z. Huang, Y. Zou and C. Yang, *Adv. Mater.*, 2022, **34**, e2106954.
34 D. Li, M. Li, W. Li, W. Li, Z. Chen, X. Peng, D. Liu, G.-X. Yang, S. Jiang, Y. Gan, Z. Yang, K. Liu and S.-J. Su, *Chem. Eng. J.*, 2023, **458**, 141416.
35 J. Wang, N. Li, C. Zhong, J. Miao, Z. Huang, M. Yu, Y. X. Hu, S. Luo, Y. Zou, K. Li and C. Yang, *Adv. Mater.*, 2023, **35**, e2208378.